ACS APPLIED MATERIALS & INTERFACES

www.acsami.org Research Article

# A Gate-Tunable Thermal Persistent Photocurrent Device for In-Sensor Spiking Neural Networks

Xiao Li, Liutianyi Zhang, Yifei Zhang, Fanxin Liu, Lin Wang,* Ping-Heng Tan,* and Jiangbin Wu*

Cite This: *ACS Appl. Mater. Interfaces* 2026, 18, 20860−20868

Read Online

ACCESS | Metrics & More | Article Recommendations | Supporting Information

**ABSTRACT:** Persistent photocurrent is widely observed in van der Waals (vdW) heterostructures and is often attributed to trap-assisted photogating, yet its microscopic origin remains unclear. Here, we clarify the mechanism in a gate-tunable $MoS_2$/black phosphorus (BP) $p-n$ heterojunction by combining DC and lock-in measurements with time-resolved decay. We simultaneously measure the general photocurrent (DC difference between illuminated and dark currents) and the net photocurrent extracted by the lock-in detection of a modulated laser. The net photocurrent is small and short-lived, whereas the DC photocurrent shows decay lifetimes ($\tau$) exceeding hundreds of seconds at negative back-gate voltage ($V_g$) but collapses rapidly for positive $V_g$ or under reverse bias. This $\tau-V_g$ and bias dependence is incompatible with a purely trap-dominated picture. We show that the long-lived response is dominated by majority-carrier recombination-induced self-heating in the forward-biased $p-n$ junction, which drives thermoelectric and bolometric currents. By tuning the heterostructure between a $p-n$ and an $n-n$ configuration, the back gate effectively switches this thermal channel on and off. Using the experimentally extracted $\tau(V_g)$ in a leaky integrate-and-fire model, we further demonstrate an in-sensor spiking neural network with 91.95% accuracy on MNIST, highlighting the potential of thermally engineered persistent-photocurrent devices for neuromorphic vision.

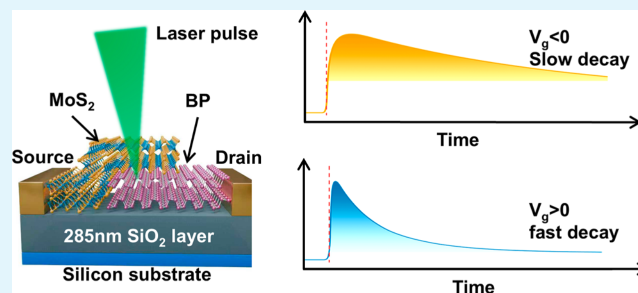


**KEYWORDS:** *persistent photocurrent, $MoS_2$/BP heterojunction, recombination-induced self-heating, thermoelectric and bolometric effects, in-sensor spiking neural networks*

## INTRODUCTION

With a great breakthrough in low-dimensional materials, the surge of vdW materials and their applications has lightened new skylines of science.[1−4] The exfoliation and flexibility of vdW materials offer us infinite probabilities to engineer exfoliated flakes with all kinds of methods, such as folding,[5−7] picking,[8] and stacking several different types of materials.[9] Among these methods, stacking different materials to fabricate a heterojunction is widely used to create electronically programmable devices with decent photoresponse.[10,11] Recently, persistent photoconductivity is observed in many experiments owing to the charge trapping effect in hybrid heterojunctions (graphene/$MoS_2$).[12] These devices maintain a long photoexcited state that hardly decays, enabling scientists to manufacture nonvolatile optical memories with great retention performance and multibit programming.[13−15]

However, the mechanisms of persistent photocurrents in such heterostructures still need to be explored. A widely adopted and experimentally convenient approach to quantify photocurrent ($I_{ph}$) is to define the photoresponse as the current difference between illuminated ($I_{illuminated}$) and dark ($I_{dark}$) conditions, $I_{ph} = I_{illuminated} - I_{dark}$.[16−18] Therefore, thermal excitation is also unavoidably included in $I_{ph}$ and plays an important role in photocurrent generation.[19] When the incident laser is periodically modulated by a mechanical chopper, the resulting photocurrent acquires the same temporal modulation. By using phase-sensitive detection in a lock-in amplifier, only the current components oscillating synchronously with the modulation frequency are extracted, while DC contributions such as dark current, slow photogating effects, and thermal drift are effectively suppressed. The resulting signal, referred to as the net photocurrent ($I_{ph}^{net}$), selectively probes the fast photoconductive response associated with intrinsic photocarrier generation and transport, independent of long-lived thermal or persistent components present in the general photocurrent.[20−22] Comparing the general photocurrent $I_{ph}$ with $I_{ph}^{net}$ is therefore essential for decoupling the contributions of photogating, photoconductive generation, and thermally driven processes to the unusually long-lived photoresponse, a distinction that is crucial for identifying the

Received: December 17, 2025
Revised: March 10, 2026
Accepted: April 1, 2026
Published: April 6, 2026

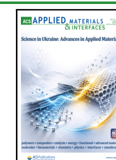

ACS Publications © 2026 American Chemical Society

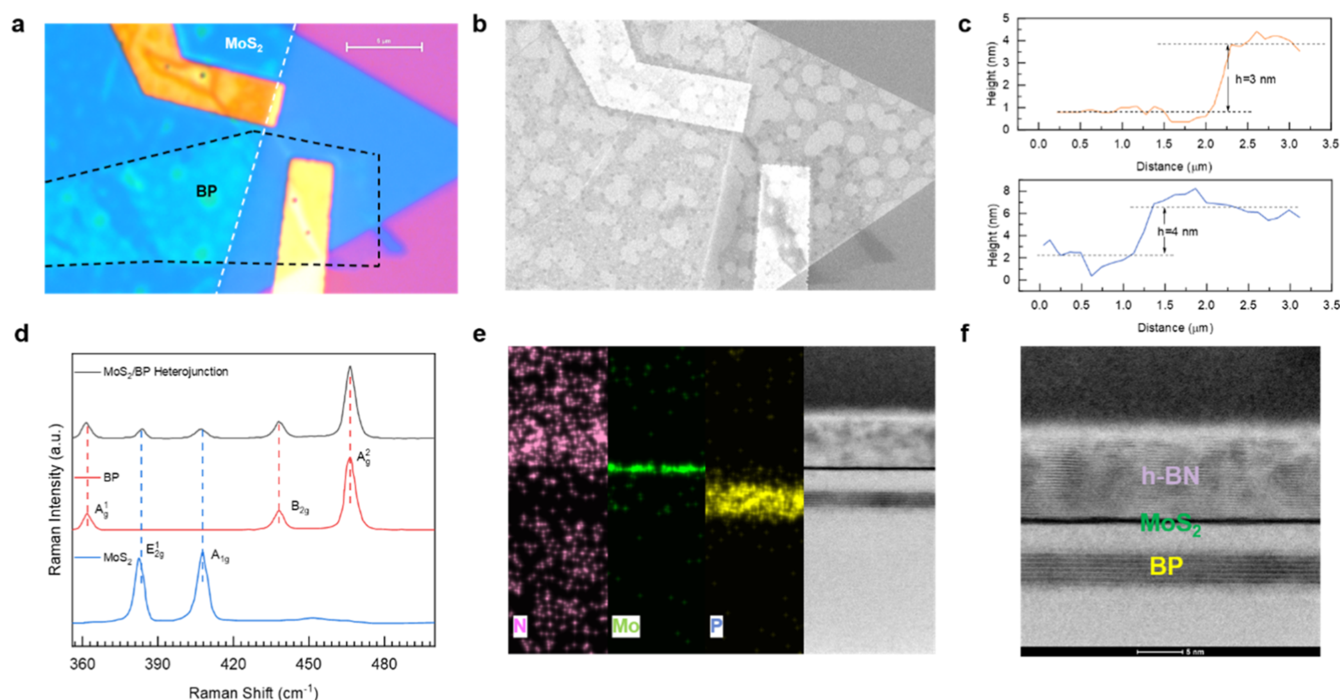


**Figure 1.** (a) Optical microscopic image of the $MoS_2$−BP heterojunction with electrodes. $MoS_2$ (white dotted line) is on the top of BP (black dotted line). (b) AFM image of the heterojunction. Blue and orange dotted lines are the height sampling lines. (c) Height profiles of $MoS_2$ and BP flakes. Top: 3 nm thickness $MoS_2$. Bottom: 4 nm thickness BP flake. (d) Raman spectra of BP, $MoS_2$, and the overlapped regions. (e) EDS elemental mapping of the encapsulated $MoS_2$−BP heterojunction, showing uniform elemental distribution and absence of oxidation-related degradation. (f) Cross-sectional STEM image of the heterostructure, confirming the well-defined layered stacking and effective h-BN encapsulation.

dominant mechanism underlying persistent photocurrent in vdW heterojunctions.

In this article, we introduce a $MoS_2$−BP $p$−$n$ heterojunction to demonstrate its photonic and electronic behaviors. Comparing the two photocurrents measured differently, we find that $I_{ph}$ dominates in most cases when we tune the back-gate voltage ($V_{bg}$). The peak dislocation between gate-dependent $I_{ph}$ and $I_{ph}^{net}$ illustrates the photogating effect clearly in our $p$−$n$ junction. The time-resolved measurements after a 2.5 s laser input show that the decay lifetime $\tau$ decreases a lot as $V_{bg}$ increases. And when a reverse bias is applied at the drain, the lifetime is quite smaller than it is under a forward bias. All the findings above suggest the thermal effect outperforms the charge trapping effect in this hardly decaying photocurrent. We propose a model to qualitatively explain the thermal effect caused by carrier recombination and its mechanism behind the persistent photoresponse, hoping to arouse more studies on the physics in photocurrent generation and to exploit further applications on optoelectronic devices. Beyond photodetection, the gate-tunable persistent photocurrent and intrinsic carrier dynamics of such heterojunctions make them compelling building blocks for neuromorphic systems—serving as optoelectronic synapses, in-sensor memory/compute units, and neuron-like spiking elements that integrate sensing, memory, and computation in a single vdW heterostructure.[23−25] In particular, by incorporating the gate-tunable persistent photocurrent dynamics into a LIF model, we demonstrate that the heterojunction can directly emulate neuronal firing and process temporally encoded signals, enabling an in-sensor spiking neural network that achieves 91.95% accuracy on the MNIST data set. This work thereby not only elucidates the photocurrent mechanism but also extends the application horizon of BP-$MoS_2$ heterostructures to bioinspired computing, demonstrating their utility in an integrated SNN for visual pattern recognition.

## Basic Characterization and Photocurrent Measurement

Here, we exfoliated a BP flake first with a transferred $MoS_2$ flake over it. Since BP is easily degraded in the ambient condition,[26] a large boron nitride (BN) covered the whole device to protect BP from degeneration. The electrodes are deposited all around the overlapped region closely to minimize the channel length, as shown in Figure 1a. We choose 3−4 nm flakes to fabricate this $p$−$n$ diode as it has a relative low gate screening effect (Figure 1b,c).[27,28] The excellent gate control of the channel lays the foundation of uniform gate tuning across BP and $MoS_2$ synchronously when we sweep $V_{bg}$. Figure 1d manifests clear featured Raman peaks in BP and $MoS_2$ separately and in the overlapped region, indicating good quality of our exfoliated flakes and fine protection from the BN covering layer against the degradation.[29,30] To further verify the structural integrity and encapsulation quality of the heterojunction, energy-dispersive X-ray spectroscopy (EDS) mapping and scanning transmission electron microscopy (STEM) characterization were performed, as shown in Figure 1e,f. The elemental mapping confirms the uniform distribution of constituent elements and the absence of oxidation-related species, while the STEM image clearly reveals a well-defined layered stacking structure. These results demonstrate that h-BN encapsulation effectively protects the BP channel from environmental degradation.

We characterize drain-source current ($I_{ds}$) and photoresponse versus $V_{bg}$ under the illumination of a 520 nm laser. The source electrode over $MoS_2$ is always grounded and drain-source voltage ($V_{ds}$) is applied on the BP side. The schematic illustration of the device is shown in Figure 2a and

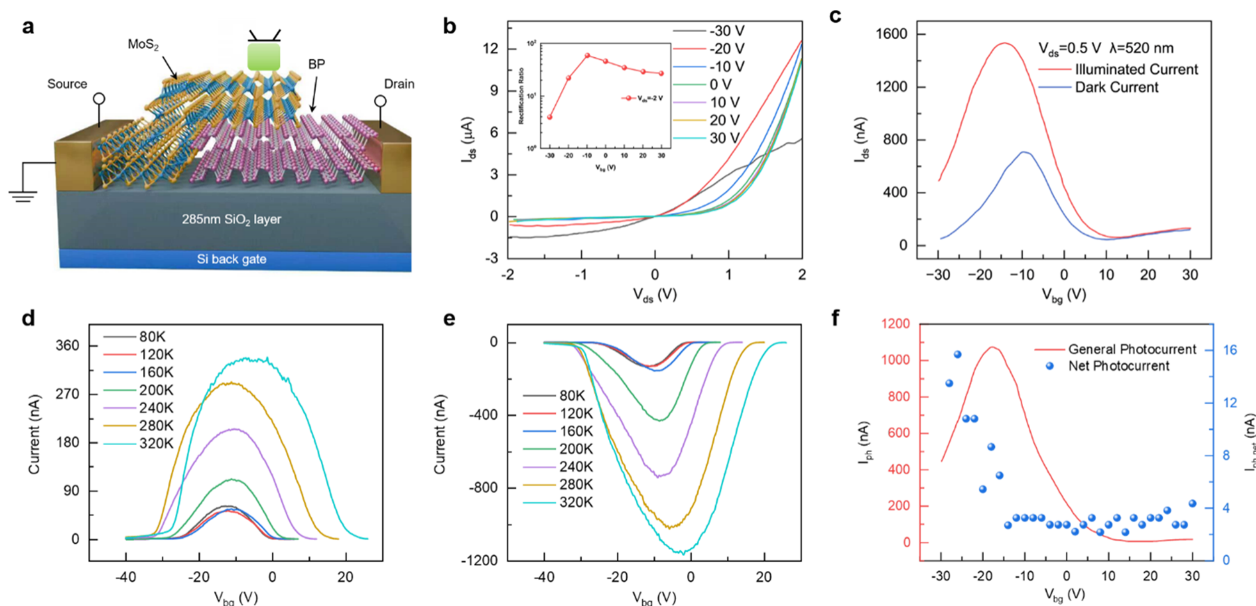


**Figure 2.** (a) Schematic illustration of the $MoS_2$−BP heterojunction under a 520 nm laser injection at the overlapped region. (b) $I_{ds}$−$V_{ds}$ characteristics under different gate voltages. Inset: Rectification ratio under different gate voltages. (c) Gate-dependent $I_{ds}$ at $V_{ds}$ = 0.5 V with and without laser illumination ($\lambda$ = 520 nm, laser power = 6.3 $\mu$W). (d,e) Temperature-dependent transfer characteristics ($I_{ds}$−$V_{bg}$) of the $MoS_2$−BP heterojunction measured under dark conditions at the same drain bias. Increasing temperature leads to an enhanced on-state current and a broadened current peak, indicating thermally activated transport and supporting a thermal contribution to the persistent photoresponse. (f) Gate-dependent net photocurrent $I_{Ph,net}$ and general photocurrent $I_{ph}$ at frequency $f$ = 20 Hz and $V_{ds}$ = 0.5 V.

the laser is spotted at the overlapped region to equalize the distance to both electrodes for photoexcited carriers. As shown in the schematic, the channel is made up of three parts: nonoverlapped BP region, $MoS_2$−BP overlapped region, and nonoverlapped $MoS_2$ region. Transfer characteristics are shown in Figure 2b.

Exfoliated $MoS_2$ is usually an $n$-type material while exfoliated BP is a $p$-type material.[31,32] So, all of the measurements show a rectification behavior as a $p$−$n$ diode. The rectification ratio grows when $V_{bg}$ increases from −30 V (the ratio <10 at $V_{bg}$ = −30 V) and reaches the peak at around $V_{bg}$ = −10 V (around 1 × $10^2$). Then the rectification ratio slightly drops to ∼30 as $V_{bg}$ increases to a positive value. This nonmonotonic evolution arises from the gradual reduction of hole concentration in BP as the gate voltage shifts from negative to positive values. When $V_{bg}$ > −10 V, the weakening $p$-type character of BP reduces the built-in potential of the $p$−$n$ junction, leading to a suppressed rectification behavior (inset of Figure 2b).[33] The gate-dependent $I_{ds}$ are plotted in Figure 2c in dark conditions and in illuminated conditions, respectively, under the $V_{ds}$ = 0.5 V. In dark conditions, we see a peaking-down curve when $V_{bg}$ sweeps across from −30 V to 30 V. To directly probe the thermal contribution to charge transport, we further performed temperature-dependent electrical measurements under dark conditions. Figure 2d,e shows the transfer characteristics measured at different temperatures under the same drain bias. With increasing temperature, the on-state current of the heterojunction increases monotonically, accompanied by a gradual broadening of the gate-voltage range, over which the current peak appears. Such behavior is consistent with thermally activated transport and an enhanced carrier population, indicating that the channel conductivity is sensitive to temperature variation. This temperature dependence provides direct experimental evidence that thermal effects can significantly modulate the electrical response of the $MoS_2$−BP heterojunction, supporting the thermal origin of the persistent photocurrent discussed below. When −30 V < $V_{bg}$ −10 V, at the beginning, the nonoverlapped $n$-type $MoS_2$ channel is fully depleted and BP is highly $p$-doped under large negative gate voltage. So, the depleted $MoS_2$ channel cuts off the current. As $V_{bg}$ gradually increases, the back gate turns on the $MoS_2$ channel in both the non-overlapped and overlapped regions, which contributes to the current increasing. $I_{ds}$ peaks at $V_{bg}$ = −10 V when $MoS_2$ and BP are both turned on. When −10 V < $V_{bg}$ < 10 V, the $MoS_2$ channel is opening but BP is starting to be depleted. The decreasing BP current dominates, resulting in the decline of $I_{ds}$. When $V_{bg}$ > 10 V, $MoS_2$ is greatly $n$-doped, but the dominating current here is the $n$-doped BP. The ambipolar switching of BP weighs in due to the saturation of $MoS_2$ current in large positive gate voltage and $I_{ds}$ begins to slightly increase (results in agreement with the similar $MoS_2$/BP heterojunction).[34] Under illumination conditions, $I_{ds}$ almost follows the same tendency. The current peak shifts mildly because of the gate capacitance charge storage.[35] Thus, we could obtain the general photocurrent by defining $I_{ph}$ = $I_{illuminated}$ − $I_{dark}$, which peaks at around $V_{bg}$ = −15 V (Figure 2f). The gate-dependent evolution of the photocurrent jump amplitude and its temporal decay behavior are further illustrated by the time-resolved measurements shown in Figures S1 and S2. Furthermore, photocurrent measurements under different laser power densities (Figure S3) reveal a monotonic increase in the photocurrent amplitude with increasing optical power, confirming that the device response follows the expected photogeneration behavior without altering the underlying decay mechanism.

Then, we use a rotating chopper to modulate the injected laser at 20 Hz and a dynamic analyzer (see the Methods) to only detect the net photocurrent $I_{ph}^{net}$ caused by the photoconductive effect, which offers enough energy to excite electrons over the band gap and generate an electron−hole


https://doi.org/10.1021/acsami.5c25164
ACS Appl. Mater. Interfaces 2026, 18, 20860−20868

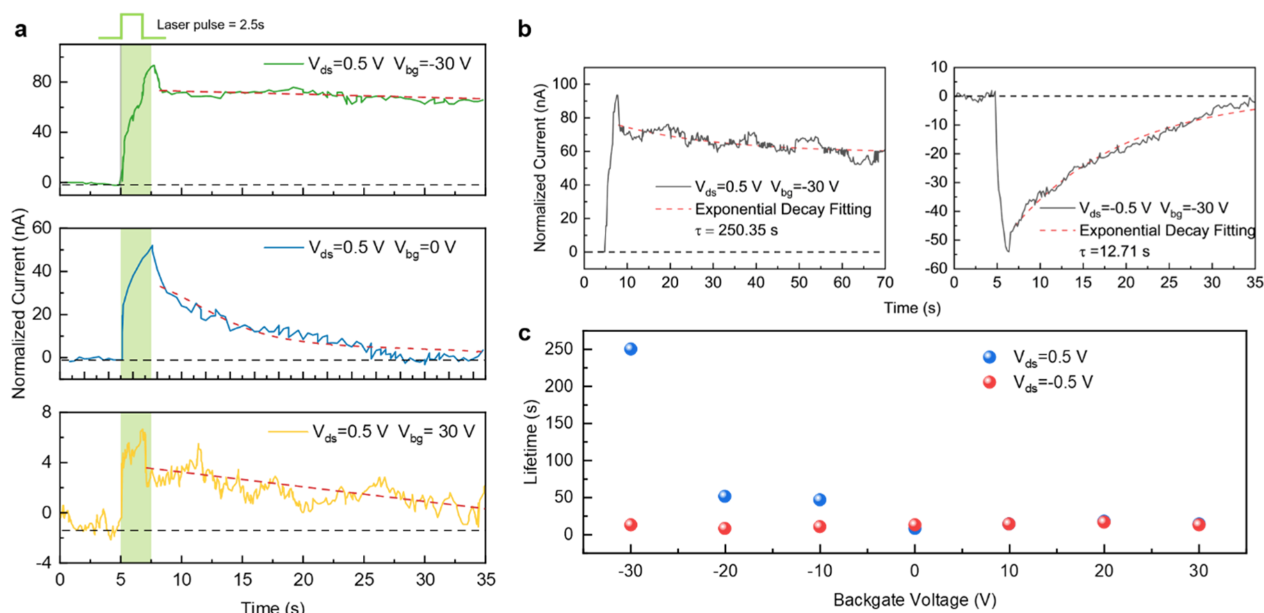


**Figure 3.** (a) Time evolution measurement of the normalized current after a 2.5 s laser pulse under $V_{bg}$ = −30 V, 0 V, and 30 V. The black dotted line is the base current normalized by the stable current before the laser pulse input. The red dotted line is the exponential fitting decay after the laser pulse is over. (b) Left: Extended time evolution measurement of the normalized current up to 70 s under $V_{bg}$ = −30 V and $V_{ds}$ = 0.5 V. Right: Time evolution measurement of the normalized current under $V_{bg}$ = −30 V and $V_{ds}$ = −0.5 V. (c) Gate-tuned lifetime of the photocurrent under forward bias and reverse bias.

pair to drift under the external electric field.[36] Photoconductive effect-caused $I_{ph}^{net}$ is determined by several parameters, including photoinduced carrier density $n_{e/h}^{*}$ and transit time $\tau_{tr}$ that photoinduced carriers take to transit through the channel toward electrodes before annihilation.[37] The average drift velocity $v = \mu E$, where $\mu$ is the carrier mobility and $E$ is the external electric field, and $\tau_{tr} = L/\mu E$, where $L$ is the distance from the laser spot to the electrode.[38] So, when the back gate tunes carrier density and mobility in the heterojunction, $I_{ph}^{net}$ is supposed to follow the same peaking-down curve as $I_{ds}$ and $I_{ph}$ do. However, $I_{ph}^{net}$ shows almost a constant decreasing trend as the $V_{bg}$ varies from −30 V to 30 V. This shift indicates the presence of a photogating effect (Figure 2f). Photogenerated carriers are trapped by localized traps states that originate from dangling bonds and defects, which are mostly distributed within the band gap.[39] These trapped carriers act as a local gate to screen the back gate tuning and shift the threshold voltage $V_{th}$. These charge traps will prolong the recombination lifetime $\tau_{net}$ of the photogenerated carriers instead. As long as $\tau_{net}$ is longer than $\tau_{tr}$, there will be more carriers that could transit to the electrode before they annihilate due to the recombination, which leads to a larger photoresponse gain $\tau_{net}/\tau_{tr}$.

Despite these benefits of the charge trapping effect, $I_{ph}^{net}$ (around 10 nA) in our device is relatively small compared to $I_{ph}$ (over 100 nA) here. Because the exfoliated flakes are not thick enough to achieve strong light absorption and the incident laser power used here is also relatively low, the resulting photocurrent is lower than that reported in previous studies (over 10 nm flake and over 200 $\mu$W laser power).[20] In addition, temperature-dependent photoresponse measurements performed at 100, 200, and 300 K show consistent decay dynamics and persistent photocurrent behavior (Figure S4), indicating that the observed long-lived photocurrent is intrinsic to the heterojunction rather than dominated by environmental adsorbates. Meanwhile, the long distance from the illuminated area to the electrodes will also increase $\tau_{tr}$, promoting the possibility of annihilation. So, $I_{ph}^{net}$ and the photogating effect do not dominate in the persistent photoresponse.

## Lifetime Tuned by the Gate and Proposed Mechanism

In order to elaborate the dominating mechanism, we investigate the time evolution of normalized $I_{ds}$, where we define the stable current before the laser pulse as the baseline and subtract it to obtain a more explicit view of the change after the laser pulse injection. First, we applied a forward bias of $V_{ds}$ = 0.5 V. In Figure 3a, we see a sharp increase when the laser is turned on due to the generated photocurrent and an immediate drop when the laser is shuttered. The drop is several nanoamperes in milliseconds, which conforms to the value and lifetime of $I_{ph}^{net}$. Then, the normalized current decays slowly when $V_{bg}$ = −30 V and declines much faster when $V_{bg}$ increases to the positive value ($V_{bg}$ = 30 V). Moreover, the step change in photocurrent also decreases as $V_{bg}$ increases (more figures are provided in Supporting Information S1). This is reasonable behavior that complies with our measurement of $I_{ph}$ in Figure 2f. Because, at $V_{bg} > 0$, the $MoS_2$ channel is depleted and the carrier density is low so that $I_{ph}$ is weak.

We did an exponential fitting for the decay of normalized currents under different $V_{bg}$. The function $I_{ds} = A_0 + A_1\exp(-t/\tau)$ shows lifetime $\tau$ = 250.35 s at $V_{bg}$ = −30 V and $\tau$ = 13.34 s at $V_{bg}$ = 30 V. The lifetime of the general photocurrent $I_{ph}$ is significantly longer than the net photocurrent lifetime $\tau_{net}$. Therefore, there are more factors beyond the photogating effect and charge trapping effect to form this persistent photocurrent. We also measured the time-dependent normalized current at a reverse bias $V_{ds}$ = −0.5 V and compared these two curves when $V_{bg}$ = −30 V (Figure 3b). The lifetime $\tau$ of $I_{ph}$ under reverse bias is significantly shorter (12.71 s) than that under forward bias (250.35 s). This pronounced asymmetry primarily originates from the built-in electric field of the $MoS_2$−BP $p$−$n$ heterojunction, which strongly modulates


https://doi.org/10.1021/acsami.5c25164
ACS Appl. Mater. Interfaces 2026, 18, 20860−20868

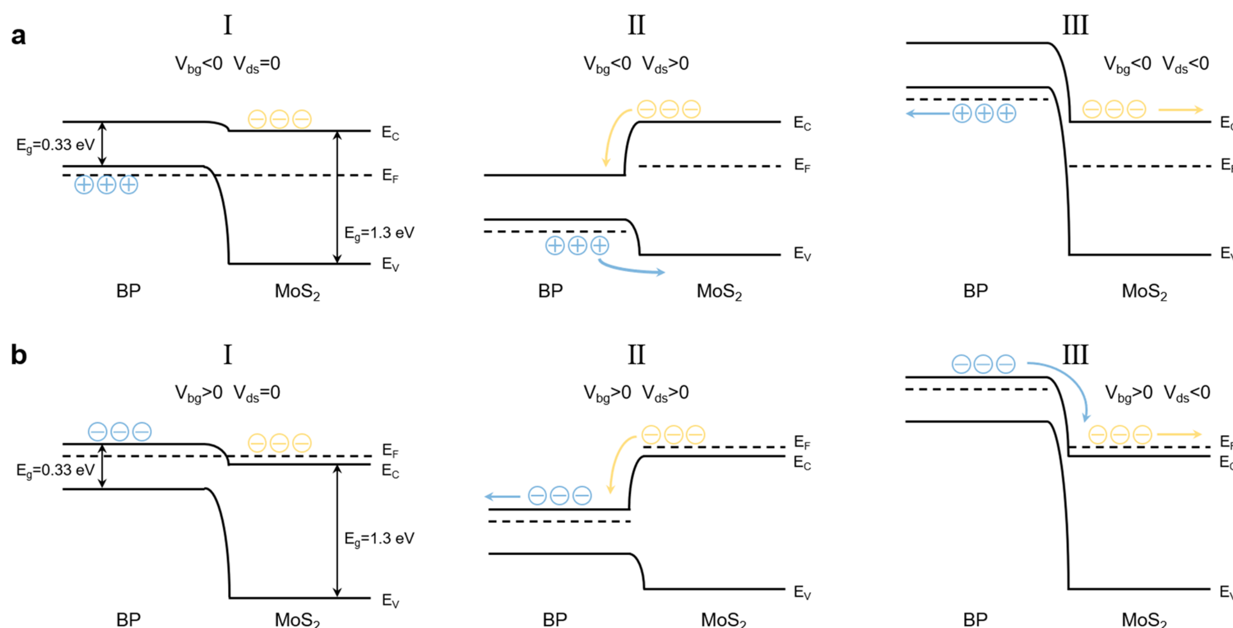


**Figure 4.** (a) Schematics of band profiles under negative $V_{bg}$. (I) $V_{ds}$ = 0. (II) $V_{ds}$ > 0. (III) $V_{ds}$ < 0. Valence band $E_V$, conductive band $E_C$, Fermi level $E_F$, and band gap $E_g$ are labeled. Blue plus particles are the holes in BP. Orange minus dots are the electrons in $MoS_2$. Arrows indicate the carrier flow direction under an external electrical field. (b) Schematics of band profiles under positive $V_{bg}$. (I) $V_{ds}$ = 0. (II) $V_{ds}$ > 0. (III) $V_{ds}$ < 0. Blue minus particles are the holes in BP. Orange minus dots are the electrons in $MoS_2$.

carrier recombination at the depletion region. Under forward bias, the junction field promotes electron−hole recombination, leading to sustained self-heating and a prolonged photoresponse, whereas reverse bias suppresses recombination and rapidly quenches the thermal contribution. Contact-related effects are expected to play a secondary role, as the gate-dependent lifetime trends are consistently observed across different bias polarities (Supporting Information, Figure S2). Figure 3c shows that $\tau$ decreases notably as $V_{bg}$ increases, reflecting a transition in the dominant carrier type and recombination pathways within the heterojunction. At negative gate voltages, BP remains *p*-type, while $MoS_2$ is *n*-type, enabling efficient majority-carrier recombination at the depletion region and giving rise to sustained self-heating. As $V_{bg}$ increases and the heterostructure evolves toward an *n*−*n* configuration, majority-carrier recombination is progressively suppressed, leading to a rapid collapse of the thermal channel and a shortened photocurrent lifetime.

Amid the great efforts to explore the application of 2D materials with a wide range of the spectrum, scientists already notice the sophisticated interaction of photon, phonon, and electron.[40−42] The origin of photocurrent in optoelectronic devices undergoes numerous investigations as the energy relaxation of the excited carriers and laser-induced photons will dissipate into thermal sinks, which will in reverse drive a thermal current.[19] This is the key issue to maintain a persistent photocurrent with a long lifetime. Our $MoS_2$−BP heterojunction provides a perfect opportunity to figure out the mechanism behind the lifetime-tuned photocurrents. Multilayer BP has a small band gap ($E_g$) in the infrared region with $E_g$ = 0.33 eV and $MoS_2$ is also a transition metal dichalcogenides material with a layer-dependent band structure.[43,44] Exfoliated multilayer $MoS_2$ has an indirect band gap with $E_g$ = 1.3 eV. Because we have an overall global Si back gate, when $V_{bg}$ is highly negative, both $MoS_2$ and BP Fermi level $E_F$ lower down (Figure 4a part I). Original $MoS_2$ is *n*-doped and negative gate tuning will not thoroughly change $MoS_2$ into a *p*-doped material. Therefore, under $V_{bg}$ = −30 V, the majority carrier of $MoS_2$ is an electron, while the majority carrier of BP is a hole. Bias voltage is applied on the drain electrode. Applied forward bias will lower the energy level in the BP side. Driven by the external electric field, holes from BP and electrons from $MoS_2$ will drift in the opposite direction toward the depletion region lying in this *p*−*n* diode (Figure 4a part II). These two types of carriers (not the photoexcited carriers) will annihilate when they meet opposite charges. Such recombination will release energy and heat a certain area. Microscopically, the energy releasing during this recombination will result in carrier emission ultimately, like Auger effect and lattice-relaxation multiphonon emission.[45,46] In contrast, reverse bias will drive holes and electrons away from each other so that the recombination rate will drop significantly (Figure 4a part III). Without the carrier recombination, there will be no self-heating at the depletion region. The laser-induced photocurrent and thermal excitation will dissipate quickly at the reverse bias.

If we investigate this self-heating effect macroscopically, the recombination area will cause a temperature difference between BP and $MoS_2$ flakes at the interface owing to their different thermal conductivity.[47,48] Subsequently, the thermal current will be driven via thermoelectric and bolometric processes. Current generated by the thermoelectric effect could be formulated as follows: $I = (S_2 - S_1) \cdot \Delta T / R$, where $S$ is the thermoelectric power, $\Delta T$ is the temperature difference, and $R$ is the average resistance of the heterostructure.[49] Moreover, the bolometric process via local heating could produce a resistance difference in two flakes, contributing to another thermal current part.[18] Conclusively, the laser-induced heating effect will disappear soon after the laser is shuttered, while the recombination of the opposite majority of carriers in *n*-type $MoS_2$ and *p*-type BP will constantly release energy to maintain the current level as long as the bias voltage is applied during


https://doi.org/10.1021/acsami.5c25164
ACS Appl. Mater. Interfaces 2026, 18, 20860−20868

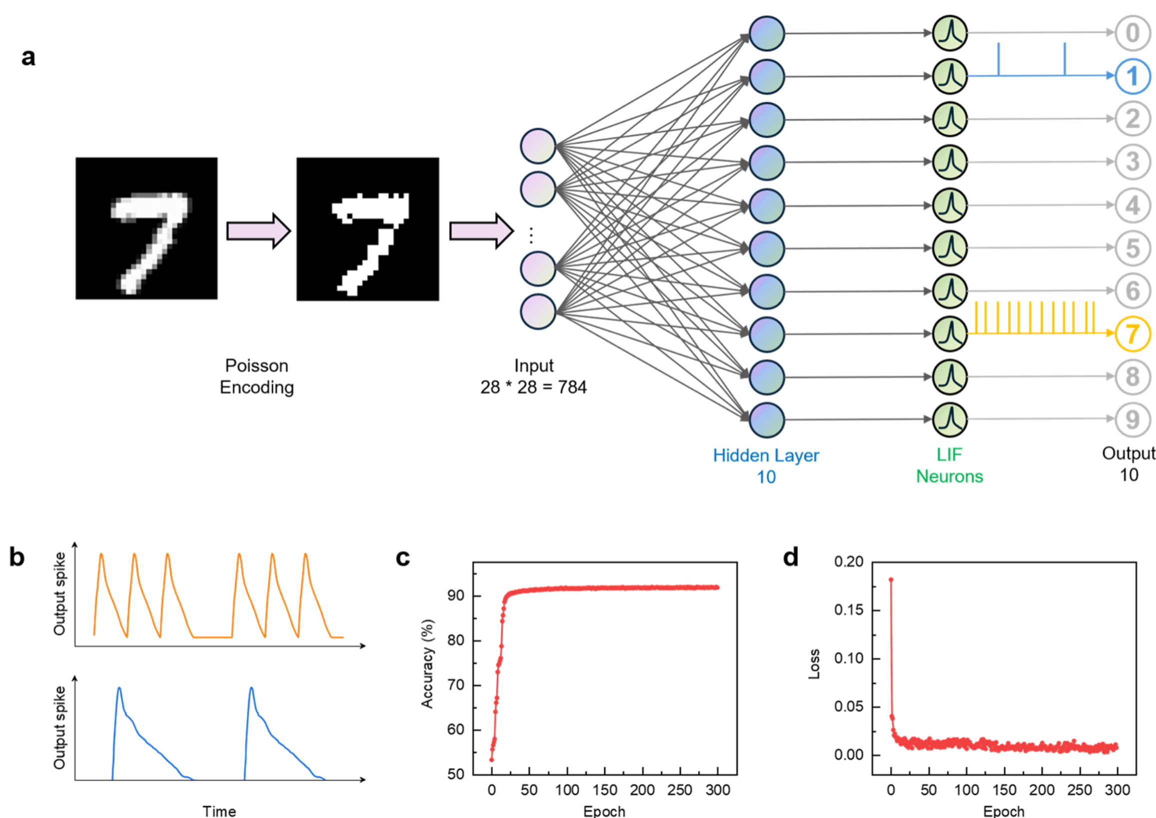


**Figure 5.** (a) Schematic of the SNN processing the neuromorphic MNIST data set. (b) Output spike signals for correct and incorrect classifications. The blue trace (low frequency) corresponds to an incorrect result ("1"), while the orange trace (high frequency) represents the correct classification ("7"). (c) Training accuracy and (d) corresponding loss during training of the BP/$MoS_2$-based SNN.

the time evolution measurement. We believe our model, in which carrier recombination heats a localized region and generates a thermal current, explains the sustained photocurrent over hundreds of seconds. As $V_{bg}$ is gradually swept from negative to positive values, BP begins to transition toward n-type conduction, while $MoS_2$ remains *n*-type (Figure 4b part I). Then the majority of carriers in BP and $MoS_2$ is electron. No matter how the bias is applied, there will be no electron−hole recombination to sustain the current level (Figure 4b parts II and III). The homogeneity of carriers results in the same drifting direction in two materials. The lifetime $\tau$ of $I_{ph}$ will consequently decrease quickly as $V_{bg}$ increases. To further explore the neuromorphic computing potential of our BP/$MoS_2$ heterojunction device, we implemented an SNN architecture that leverages the intrinsic device dynamics. The heterojunction exhibits gate-tunable persistent photoconductivity and carrier recombination characteristics, which enable it to emulate LIF neuron behavior with native temporal processing capabilities. This makes it particularly suitable for processing temporal signals encoded in the spiking domain. Notably, the demonstrated LIF behavior originates from the gate-tunable photocurrent relaxation dynamics rather than from a material-specific property of the BP−$MoS_2$ system, suggesting that this approach can be generalized to other vdW heterojunctions exhibiting a persistent photoresponse. We adopted a Poisson-encoding scheme to convert the MNIST handwritten digit data set into an asynchronous, sparse, binary spike format. This encoding strategy transforms each pixel's grayscale value into a corresponding firing rate, producing spike trains distributed across multiple time steps. Such temporal encoding preserves rich spatial and intensity information in the form of timing sequences, making it compatible with the temporal dynamics of our memristive heterojunction.[50,51] For example, as illustrated in Figure 5a, each pixel of the digit "7" is represented as a binary spike sequence over time, collectively forming 784 parallel input channels to the SNN. The network performs classification based on the output neuron with the highest spike count, where correctly classified digits elicit higher firing rates. As shown in Figure 5b, the orange trace—representing the correct classification of digit "7"—displays a denser spike pattern, while the blue trace (incorrect classification, "1") shows sparse activity. This frequency-based decision mechanism aligns well with the heterojunction's ability to sustain and differentiate rate-coded inputs. Through supervised learning, the BP/$MoS_2$-based SNN achieved a recognition accuracy of 91.95% (Figure 5c) with a final loss of 0.0056 (Figure 5d). The high accuracy and low loss underscore the device's efficiency in processing temporally encoded information and its suitability for neuromorphic implementations. These results highlight the potential of BP-$MoS_2$ heterojunctions in building energy-efficient, non-von Neumann computing systems for complex pattern recognition tasks.

## CONCLUSIONS

In summary, we fabricated a $MoS_2$−BP *p*−*n* heterojunction whose lifetime could be significantly tuned by the back gate, ranging from over 250 s to around 10 s. The device manifests a good rectification ratio and gate-tuned $I_{ds}$. Unlike the traditional way, we not only characterize the general photocurrent by defining $I_{ph} = I_{illuminated} - I_{dark}$, but we also modulate the injected 520 nm laser and obtain the net

photocurrent as well. $I_{Ph,net}$ measured by the standard lock-in amplifier technique reflects the photogating effect but possesses a small value and a short lifetime $\tau_{net}$, indicating a nondominant role in the persistent photocurrent here. A key finding of this work is that the long-lived photocurrent at negative gate bias ($V_{bg}$ = −30 V, $\tau$ > 250 s) arises primarily from majority-carrier recombination-induced self-heating in the forward-biased $p$−$n$ junction. When $V_{bg}$ < 0 V, $MoS_2$ remains $n$-type and BP remains $p$-type, enabling electron-hole recombination near the depletion region under forward bias ($V_{ds}$ > 0 V). This recombination continuously releases heat, generating a persistent thermoelectric and bolometric current that sustains the photocurrent long after the laser is turned off. As $V_{bg}$ increases and the heterostructure evolves toward an $n$−$n$ configuration, majority-carrier recombination is suppressed and the thermal channel collapses, leading to a rapid decrease in $\tau$. This gate-controlled thermal mechanism, rather than photogating, is thus identified as the dominant driver of the persistent photoresponse in the $MoS_2$−BP heterojunction.[52] This lifetime-tuned heterojunction provides a valuable platform to further investigate the mechanism of photocurrent generation. More characterization techniques are expected to quantitively analyze the thermoelectric and bolometric processes, which could clear the obstacles toward the origin of photocurrents. Notably, the gate-tunable dynamics of the heterojunction also enable its use as an artificial neuron in SNNs. We demonstrated a proof-of-concept MNIST classification system using the heterojunction as an LIF neuron, achieving a recognition accuracy of 91.95% with low loss. This result underscores the potential of BP−$MoS_2$ devices not only in nonvolatile optical memory but also in energy-efficient neuromorphic computing. Eventually, we hope to develop a better nonvolatile optical memory with excellent retention and endurance for future semiconductor industry.

## ■ METHODS

### Device Fabrication and Basic Characterizations

All flakes were exfoliated from bulk onto a polydimethylsiloxane (PDMS) mat first and then transferred to a 285 nm $SiO_2$/$p$-doped Si substrate. With a PMMA coating, the sample went through electron beam lithography (EBL) writing. A 5 nm Cr/30 nm Au electrode was then deposited via a thermal evaporator, followed by a boron nitride (BN) covering for protection. Annealing at 280 °C was processed in a pure Ar environment for an hour to increase the interface contact. The thickness of materials was determined by an atomic force microscope (Bruker Dimension Icon). High-resolution scanning transmission electron microscopy (HR-STEM) was performed using an FEI Titan G2 system equipped with a spherical aberration corrector and four independent detectors. Prior to imaging, the sample stack was sequentially coated with chromium and carbon layers. Subsequently, the specimen was thinned using an FEI Helios 450S focused ion beam system operated at 30 keV. The HR-STEM images were acquired at an accelerating voltage of 200 keV. Transfer characteristics were performed at room temperature by Lakeshore cryogenic probe station TTPX with a Keysight B1500A analyzer.

### Raman Spectroscopy

A Renishaw inVia Qontor Raman microscope equipped with a 532 nm excitation laser, a ×100 objective, and an 1800 gr/mm grating was used to acquire the Raman spectra of the $MoS_2$−BP heterostructure. The spectral resolution was approximately 0.6 $cm^{-1}$ per pixel under these conditions. To avoid sample heating—particularly in the BP region—the excitation power was maintained below 0.3 mW throughout all measurements.

### Net Photocurrent Measurement

To isolate the fast photoconductive component of the device response, the incident 520 nm laser (= 6.3 $\mu$W at the sample surface) was periodically modulated using a Thorlabs mechanical chopper operating at a reference frequency of 20 Hz. The modulated beam was focused onto the $MoS_2$−BP overlap region, and the resulting photocurrent was detected by using a Stanford Research Systems SR844 high-frequency lock-in amplifier. The reference signal from the chopper controller was simultaneously supplied to the lock-in amplifier, enabling phase-sensitive demodulation at the modulation frequency. Through synchronous detection, the lock-in selectively extracts the first-harmonic AC component of the photocurrent that oscillates in phase with the optical modulation, while effectively rejecting the DC dark current, thermally induced background, slow photogating-related drift, and low-frequency noise. As a result, the measured signal represents the net photocurrent $I_{ph}^{net}$, corresponding exclusively to the rapid photoconductive response associated with photocarrier generation and transport. The device was connected to the lock-in amplifier through shielded coaxial cables to minimize parasitic interference, and an integration time of 1 s was used to ensure a stable signal-to-noise ratio. All measurements were carried out at room temperature under ambient conditions.

## ■ ASSOCIATED CONTENT

### Supporting Information

The Supporting Information is available free of charge at https://pubs.acs.org/doi/10.1021/acsami.5c25164.

Figures S1−S4: gate-dependent normalized photocurrent transients under forward and reverse bias; time-resolved photoresponse evolution across $V_{bg}$ = −40 to 40 V; optical power-dependent photocurrent dynamics; and temperature-dependent photoresponse measurements (100−300 K) (PDF)

## ■ AUTHOR INFORMATION

### Corresponding Authors

**Lin Wang** − *State Key Laboratory of Flexible Electronics (LoFE), School of Flexible Electronics (Future Technologies) & Institute of Advanced Materials (IAM), Nanjing Tech University (NanjingTech), Nanjing 211816, China;* orcid.org/0000-0003-3033-4792; Email: iamlwang@njtech.edu.cn

**Ping-Heng Tan** − *State Key Laboratory of Semiconductor Physics and Chip Technologies, Institute of Semiconductors, Chinese Academy of Sciences, Beijing 100083, China; Center of Materials Science and Optoelectronics Engineering, University of Chinese Academy of Sciences, Beijing 100049, China;* orcid.org/0000-0001-6575-1516; Email: phtan@semi.ac.cn

**Jiangbin Wu** − *State Key Laboratory of Semiconductor Physics and Chip Technologies, Institute of Semiconductors, Chinese Academy of Sciences, Beijing 100083, China; Center of Materials Science and Optoelectronics Engineering, University of Chinese Academy of Sciences, Beijing 100049, China;* orcid.org/0000-0002-8751-7082; Email: jbwu@semi.ac.cn

### Authors

**Xiao Li** − *State Key Laboratory of Flexible Electronics (LoFE), School of Flexible Electronics (Future Technologies) & Institute of Advanced Materials (IAM), Nanjing Tech University (NanjingTech), Nanjing 211816, China*

**Liutianyi Zhang** − *State Key Laboratory of Semiconductor Physics and Chip Technologies, Institute of Semiconductors, Chinese Academy of Sciences, Beijing 100083, China; Center of Materials Science and Optoelectronics Engineering, University of Chinese Academy of Sciences, Beijing 100049, China; School of Advanced Interdisciplinary Sciences, University of Chinese Academy of Sciences, Beijing 101408, China*

**Yifei Zhang** − *State Key Laboratory of Semiconductor Physics and Chip Technologies, Institute of Semiconductors, Chinese Academy of Sciences, Beijing 100083, China; Center of Materials Science and Optoelectronics Engineering, University of Chinese Academy of Sciences, Beijing 100049, China*

**Fanxin Liu** − *Department of Applied Physics, Zhejiang University of Technology, Hangzhou 310014, China;* orcid.org/0000-0003-0445-3886

Complete contact information is available at: https://pubs.acs.org/10.1021/acsami.5c25164

## Notes

The authors declare no competing financial interest.

## ACKNOWLEDGMENTS

The authors acknowledge support from the National Key Research and Development Program of China (Grant Nos. 2024YFA1409700, 2023YFA1407000, 2020YFA0308900, and 2022YFB3602800), the Strategic Priority Research Program of the Chinese Academy of Sciences (Grant No. XDB0460000), the National Natural Science Foundation of China (Grant Nos. 12322401, 12127807, 12393832, 62374158, 62561160153, 92477123, 52373290, and 62288102), the Beijing Natural Science Foundation (Grant no. F251001), and the Natural Science Foundation of Zhejiang Province (No. LZ22A040008).

## REFERENCES

(1) Sun, Y.; Ding, Y.; Xie, D. Mixed-dimensional van der Waals heterostructures enabled optoelectronic synaptic devices for neuromorphic applications. *Adv. Funct. Mater.* **2021**, *31*, 2105625.

(2) Liu, H.; Wu, J.; Ma, J.; Yan, X.; Yang, N.; He, X.; He, Y.; Zhang, H.; Hsu, T.-H.; Qian, J. H.; et al. A van der Waals interfacial junction transistor for reconfigurable fuzzy logic hardware. *Nat. Electron.* **2024**, *7*, 876−884.

(3) Zhang, L.; Tan, P.-H.; Wu, J. Reconfigurable devices based on two-dimensional materials for logic and analog applications. *J. Semicond.* **2025**, *46*, 071701.

(4) Akinwande, D.; Huyghebaert, C.; Wang, C.-H.; Serna, M. I.; Goossens, S.; Li, L.-J.; Wong, H.-S. P.; Koppens, F. H. Graphene and two-dimensional materials for silicon technology. *Nature* **2019**, *573*, 507−518.

(5) Aditya, A.; Mishra, A.; Baradwaj, N.; Nomura, K.-I.; Nakano, A.; Vashishta, P.; Kalia, R. K. Wrinkles, ridges, miura-ori, and moire patterns in $MoSe_2$ using neural networks. *J. Phys. Chem. Lett.* **2023**, *14*, 1732−1739.

(6) Katiyar, A. K.; Hoang, A. T.; Xu, D.; Hong, J.; Kim, B. J.; Ji, S.; Ahn, J.-H. 2D materials in flexible electronics: recent advances and future prospectives. *Chem. Rev.* **2024**, *124*, 318−419.

(7) Miskin, M. Z.; Cortese, A. J.; Dorsey, K.; Esposito, E. P.; Reynolds, M. F.; Liu, Q.; Cao, M.; Muller, D. A.; McEuen, P. L.; Cohen, I. Electronically integrated, mass-manufactured, microscopic robots. *Nature* **2020**, *584*, 557−561.

(8) Xing, K.; McEwen, D.; Yin, Y.; Zhao, W.; Bake, A.; Cortie, D.; Liu, J.; Vu, T.-H.-Y.; Chen, Y.-H.; Hone, J.; et al. Pick-and-place transfer of arbitrary-metal electrodes for van der Waals device fabrication. *ACS Nano* **2025**, *19*, 3579−3588.

(9) Le, B. Q.; Van, T. N.; Quang, D. T.; Dinh, V. L.; Van, T. P.; Kim, N. C. T. A simple and effective carrier lifetime characterization for semiconductor thin films. *J. Semicond.* **2025**, *46*, 072101.

(10) Liu, C.; Pan, J.; Yuan, Q.; Zhu, C.; Liu, J.; Ge, F.; Zhu, J.; Xie, H.; Zhou, D.; Zhang, Z.; et al. Highly reliable van der Waals memory boosted by a single 2D charge trap medium. *Adv. Mater.* **2024**, *36*, 2305580.

(11) Kwak, I. C.; Kim, J.; Moon, J. W.; Kim, S.; Park, J. Y.; Song, O.; Mazanek, V.; Sofer, Z.; Jo, H.; Park, S. Y.; et al. Orthogonal photopatterning of two-dimensional percolated network films for wafer-scale heterostructures. *Nat. Electron.* **2025**, *8*, 235−243.

(12) Wang, C.; Chen, Y.; Ma, Q.; Suo, P.; Sun, K.; Cheng, Y.; Lin, X.; Liu, W.; Ma, G. Revealing the fundamental limit of gate-controlled ultrafast charge transfer in graphene−$MoS_2$ heterostructures. *ACS Photonics* **2024**, *11*, 5170−5179.

(13) Ames, A.; Sousa, F. B.; Souza, G. A.; de Oliveira, R.; Silva, I. R.; Rodrigues, G. L.; Watanabe, K.; Taniguchi, T.; Marques, G. E.; Barcelos, I. D.; et al. Optical memory in a $MoSe_2$/Clinochlore device. *ACS Appl. Mater. Interfaces* **2025**, *17*, 12818−12826.

(14) Ahmed, T.; Tahir, M.; Low, M. X.; Ren, Y.; Tawfik, S. A.; Mayes, E. L.; Kuriakose, S.; Nawaz, S.; Spencer, M. J.; Chen, H.; et al. Fully light-controlled memory and neuromorphic computation in layered black phosphorus. *Adv. Mater.* **2021**, *33*, No. e2004207.

(15) Pintus, P.; Dumont, M.; Shah, V.; Murai, T.; Shoji, Y.; Huang, D.; Moody, G.; Bowers, J. E.; Youngblood, N. Integrated non-reciprocal magneto-optics with ultra-high endurance for photonic in-memory computing. *Nat. Photonics* **2025**, *19*, 54−62.

(16) Yang, Y.; Pan, C.; Li, Y.; Yangdong, X.; Wang, P.; Li, Z.-A.; Wang, S.; Yu, W.; Liu, G.; Cheng, B.; et al. In-sensor dynamic computing for intelligent machine vision. *Nat. Electron.* **2024**, *7*, 225−233.

(17) Zhong, Z.; Zhuang, Y.; Cheng, X.; Zheng, J.; Yang, Q.; Li, X.; Chen, Y.; Shen, H.; Lin, T.; Shi, W.; et al. Ionic-electronic photodetector for vision assistance with in-sensor image processing. *Nat. Commun.* **2025**, *16*, 7096.

(18) Ranjan, A.; Mazumder, A.; Ramakrishnan, N. Recent advances in layered and non-layered 2D materials for UV detection. *Sens. Actuators, A* **2024**, *378*, 115837.

(19) Jiang, M.; Zhao, Y.; Bian, L.; Chen, W.; Yang, K.; Zhou, M.; Zhang, J.; Wang, Y.; Sun, H.; Lu, S. Realizing Bidirectional Photocurrent in Monolithic Dual-Mode Device for Neuromorphic Vision and Logically-Encrypted Transmission. *Adv. Funct. Mater.* **2025**, *35*, 2416288.

(20) Guo, Q.; Pospischil, A.; Bhuiyan, M.; Jiang, H.; Tian, H.; Farmer, D.; Deng, B.; Li, C.; Han, S.-J.; Wang, H.; et al. Black phosphorus mid-infrared photodetectors with high gain. *Nano Lett.* **2016**, *16*, 4648−4655.

(21) Yang, F.; Hu, Y.; Ou, J.; Li, Q.; Xie, X.; Han, H.; Cai, C.; Ruan, S.; Xiang, B. Waveguide-Integrated $MoS_2$ Field-Effect Transistors on Thin-Film Lithium Niobate with High Responsivity and Ultra-Low Dark Current. *ACS Photonics* **2025**, *12*, 2128−2136.

(22) Deakin, C.; Liu, Z. Frequency interleaving dual comb photonic ADC with 7 bits ENOB up to 40 GHz. *Proceedings of the 2022 Conference on Lasers and Electro-Optics (CLEO)*. San Jose, CA, USA, 2022; pp 1−2.

(23) Ma, H.; Fang, H.; Xie, X.; Liu, Y.; Tian, H.; Chai, Y. Optoelectronic synapses based on MXene/violet phosphorus van der waals heterojunctions for visual-olfactory crossmodal perception. *Nano-Micro Lett.* **2024**, *16*, 104.

(24) Baek, S.; Yoo, H. H.; Ju, J. H.; Sriboriboon, P.; Singh, P.; Niu, J.; Park, J.-H.; Shin, C.; Kim, Y.; Lee, S. Ferroelectric field-effect-transistor integrated with ferroelectrics heterostructure. *Advanced Science* **2022**, *9*, 2200566.

(25) Ouyang, Y.; Zhang, C.; Wang, J.; Guo, Z.; Wang, Z.; Dong, M. Gate-Tunable Dual-Mode Optoelectronic Device for Self-Powered Photodetector and Optoelectronic Synapse. *Advanced Science* **2025**, *12*, No. e2416259.

(26) Wood, J. D.; Wells, S. A.; Jariwala, D.; Chen, K.-S.; Cho, E.; Sangwan, V. K.; Liu, X.; Lauhon, L. J.; Marks, T. J.; Hersam, M. C.

Effective passivation of exfoliated black phosphorus transistors against ambient degradation. *Nano Lett.* **2014**, *14*, 6964−6970.
(27) Xia, F.; Wang, H.; Xiao, D.; Dubey, M.; Ramasubramaniam, A. Two-dimensional material nanophotonics. *Nat. Photonics* **2014**, *8*, 899−907.
(28) Ling, X.; Wang, H.; Huang, S.; Xia, F.; Dresselhaus, M. S. The renaissance of black phosphorus. *Proc. Natl. Acad. Sci. U. S. A.* **2015**, *112*, 4523−4530.
(29) Ribeiro, H. B.; Pimenta, M. A.; De Matos, C. J.; Moreira, R. L.; Rodin, A. S.; Zapata, J. D.; De Souza, E. A.; Castro Neto, A. H. Unusual angular dependence of the Raman response in black phosphorus. *ACS Nano* **2015**, *9*, 4270−4276.
(30) Xia, F.; Wang, H.; Jia, Y. Rediscovering black phosphorus as an anisotropic layered material for optoelectronics and electronics. *Nat. Commun.* **2014**, *5*, 4458.
(31) Bao, W.; Cai, X.; Kim, D.; Sridhara, K.; Fuhrer, M. S. High mobility ambipolar $MoS_2$ field-effect transistors: Substrate and dielectric effects. *Appl. Phys. Lett.* **2013**, *102*, 042104.
(32) Kufer, D.; Konstantatos, G. Highly sensitive, encapsulated $MoS_2$ photodetector with gate controllable gain and speed. *Nano Lett.* **2015**, *15*, 7307−7313.
(33) Peng, H.; Tan, P.-H.; Wu, J. Contact planarization and passivation lift tungsten diselenide PMOS performance. *J. Semicond.* **2025**, *46*, 110401.
(34) Huang, M.; Li, S.; Zhang, Z.; Xiong, X.; Li, X.; Wu, Y. Multifunctional high-performance van der Waals heterostructures. *Nature Nanotechnol.* **2017**, *12*, 1148−1154.
(35) Joshi, P.; Romero, H.; Neal, A.; Toutam, V.; Tadigadapa, S. Intrinsic doping and gate hysteresis in graphene field effect devices fabricated on $SiO_2$ substrates. *J. Phys.: Condens. Matter* **2010**, *22*, 334214.
(36) Ye, L.; Li, H.; Chen, Z.; Xu, J. Near-infrared photodetector based on $MoS_2$/black phosphorus heterojunction. *ACS Photonics* **2016**, *3*, 692−699.
(37) Freitag, M.; Low, T.; Xia, F.; Avouris, P. Photoconductivity of biased graphene. *Nat. Photonics* **2013**, *7*, 53−59.
(38) Lucovsky, G.; Schwarz, R. F.; Emmons, R. B. Transit-Time Considerations in p−i−n Diodes. *J. Appl. Phys.* **1964**, *35*, 622−628.
(39) Grancini, G.; Roldán-Carmona, C.; Zimmermann, I.; Mosconi, E.; Lee, X.; Martineau, D.; Narbey, S.; Oswald, F.; De Angelis, F.; Graetzel, M.; et al. One-Year stable perovskite solar cells by 2D/3D interface engineering. *Nat. Commun.* **2017**, *8*, 15684.
(40) Freitag, M.; Low, T.; Zhu, W.; Yan, H.; Xia, F.; Avouris, P. Photocurrent in graphene harnessed by tunable intrinsic plasmons. *Nat. Commun.* **2013**, *4*, 1951.
(41) Zhang, G.; Huang, S.; Chaves, A.; Song, C.; Özçelik, V. O.; Low, T.; Yan, H. Infrared fingerprints of few-layer black phosphorus. *Nat. Commun.* **2017**, *8*, 14071.
(42) Jin, C.; Kim, J.; Suh, J.; Shi, Z.; Chen, B.; Fan, X.; Kam, M.; Watanabe, K.; Taniguchi, T.; Tongay, S.; et al. Interlayer electron−phonon coupling in $WSe_2$/hBN heterostructures. *Nat. Phys.* **2017**, *13*, 127−131.
(43) Li, L.; Kim, J.; Jin, C.; Ye, G. J.; Qiu, D. Y.; Da Jornada, F. H.; Shi, Z.; Chen, L.; Zhang, Z.; Yang, F.; et al. Direct observation of the layer-dependent electronic structure in phosphorene. *Nature Nanotechnol.* **2017**, *12*, 21−25.
(44) Mak, K. F.; Lee, C.; Hone, J.; Shan, J.; Heinz, T. F. Atomically thin $MoS_2$: a new direct-gap semiconductor. *Phys. Rev. Lett.* **2010**, *105*, 136805.
(45) Abakumov, V.; Perel, V. I.; Yassievich, I. *Nonradiative Recombination in Semiconductors*; Elsevier, 1991; Vol. 33.
(46) Lang, D.; Henry, C. Nonradiative recombination at deep levels in GaAs and GaP by lattice-relaxation multiphonon emission. *Phys. Rev. Lett.* **1975**, *35*, 1525.
(47) Luo, Z.; Maassen, J.; Deng, Y.; Du, Y.; Garrelts, R. P.; Lundstrom, M. S.; Ye, P. D.; Xu, X. Anisotropic in-plane thermal conductivity observed in few-layer black phosphorus. *Nat. Commun.* **2015**, *6*, 8572.
(48) Sahoo, S.; Gaur, A. P.; Ahmadi, M.; Guinel, M. J.-F.; Katiyar, R. S. Temperature-dependent Raman studies and thermal conductivity of few-layer $MoS_2$. *J. Phys. Chem. C* **2013**, *117*, 9042−9047.
(49) Xu, X.; Gabor, N. M.; Alden, J. S.; Van Der Zande, A. M.; McEuen, P. L. Photo-thermoelectric effect at a graphene interface junction. *Nano Lett.* **2010**, *10*, 562−566.
(50) Ke, S.; Pan, Y.; Jin, Y.; Meng, J.; Xiao, Y.; Chen, S.; Zhang, Z.; Li, R.; Tong, F.; Jiang, B.; et al. Efficient spiking neural networks with biologically similar lithium-ion memristor neurons. *ACS Appl. Mater. Interfaces* **2024**, *16*, 13989−13996.
(51) Wang, B.; Zhang, X.; Wang, S.; Lin, N.; Li, Y.; Yu, Y.; Zhang, Y.; Yang, J.; Wu, X.; He, Y.; et al. Topology optimization of random memristors for input-aware dynamic SNN. *Sci. Adv.* **2025**, *11*, No. eads5340.
(52) Schwede, J. W.; Bargatin, I.; Riley, D. C.; Hardin, B. E.; Rosenthal, S. J.; Sun, Y.; Schmitt, F.; Pianetta, P.; Howe, R. T.; Shen, Z.-X.; et al. Photon-enhanced thermionic emission for solar concentrator systems. *Nat. Mater.* **2010**, *9*, 762−767.

CAS BIOFINDER DISCOVERY PLATFORM™
CAS BIOFINDER HELPS YOU FIND YOUR NEXT BREAKTHROUGH FASTER
Navigate pathways, targets, and diseases with precision
Explore CAS BioFinder

https://doi.org/10.1021/acsami.5c25164
*ACS Appl. Mater. Interfaces* 2026, 18, 20860−20868

# Supporting Information

## A Gate-Tunable Thermal Persistent Photocurrent Device for In-sensor Spiking Neural Networks

Xiao Li[1], Liutianyi Zhang[2,3,4], Yifei Zhang[2,3], Fanxin Liu[5], Lin Wang[1*], Ping-Heng Tan[2,3*], Jiangbin Wu[2,3*]

[1] State Key Laboratory of Flexible Electronics (LoFE), School of Flexible Electronics (Future Technologies) & Institute of Advanced Materials (IAM), Nanjing Tech University (NanjingTech), Nanjing, 211816, China

[2] State Key Laboratory of Semiconductor Physics and Chip Technologies, Institute of Semiconductors, Chinese Academy of Sciences, Beijing, 100083, China

[3] Center of Materials Science and Optoelectronics Engineering, University of Chinese Academy of Sciences, Beijing, 100049, China

[4] School of Advanced Interdisciplinary Sciences, University of Chinese Academy of Sciences, Beijing, 101408, China

[5] Department of Applied Physics, Zhejiang University of Technology, Hangzhou, 310014, China

*Corresponding author(s). E-mail(s): iamlwang@njtech.edu.cn; phtan@semi.ac.cn; jbwu@semi.ac.cn

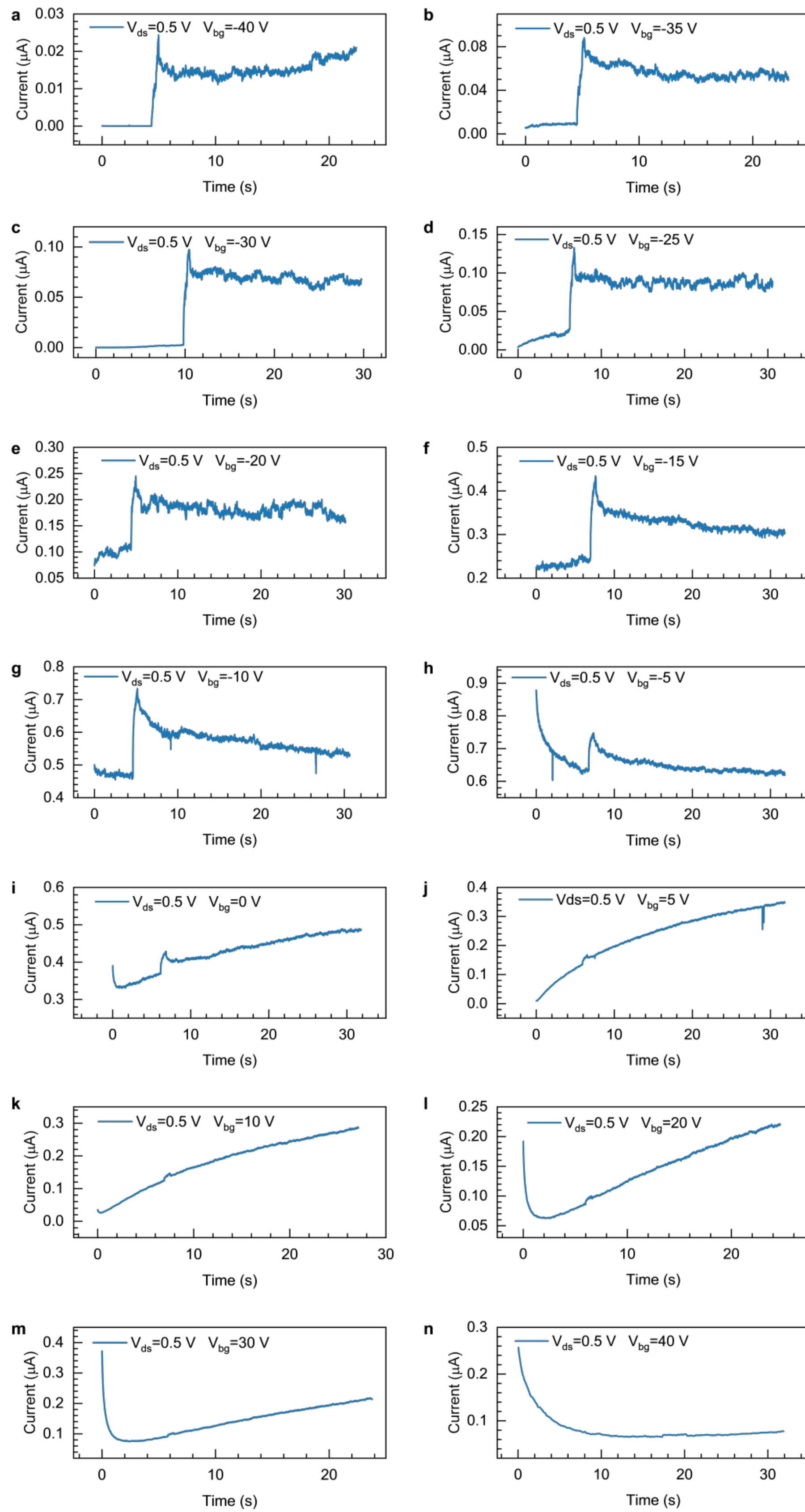


**Figure S1.** Time evolution of the normalized current following a 2.5 s laser excitation under

back-gate voltages $V_{bg}$ ranging from −40 V to 40 V. The current is normalized to its steady-state value prior to illumination. With increasing $V_{bg}$, the laser-induced photocurrent jump is progressively suppressed, reflecting a gate-controlled weakening of the photoresponse in the $MoS_2$–BP heterojunction.

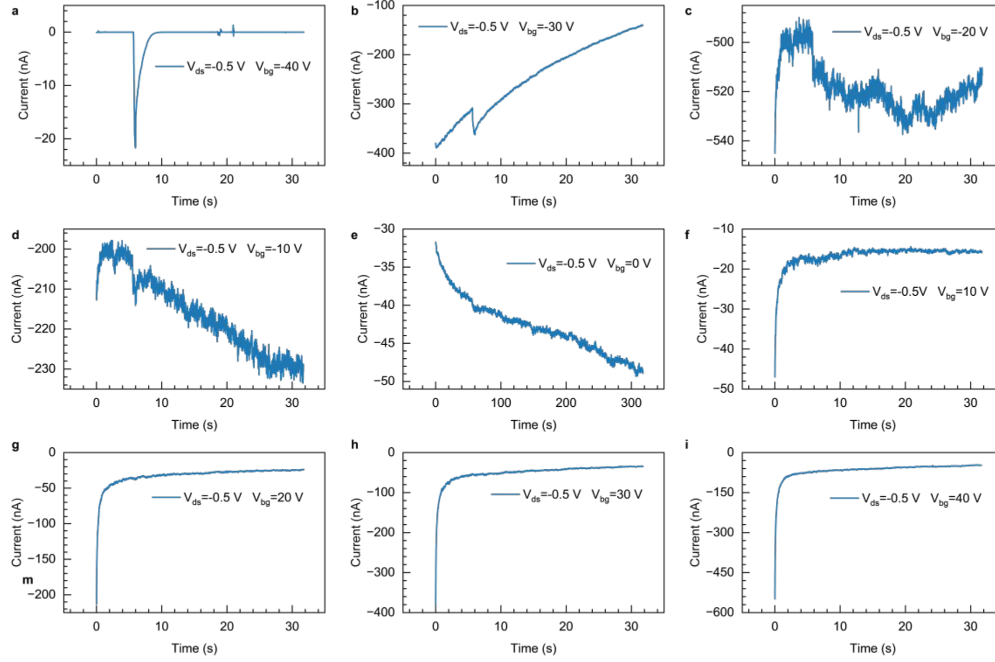


**Figure S2.** Time-resolved evolution of the normalized source–drain current measured at a reverse bias of $V_{ds}$=−0.5 V under back-gate voltages $V_{bg}$ from −40 V to 40 V. The current is normalized to the steady-state value prior to illumination. Pronounced photocurrent transients are observed for $V_{bg} < 0$, whereas the amplitude of the photoresponse progressively weakens with increasing $V_{bg}$ and becomes negligible for $V_{bg} > 0$, consistent with gate-induced suppression of carrier recombination and photoinduced current generation in the $MoS_2$–BP heterojunction under reverse bias.

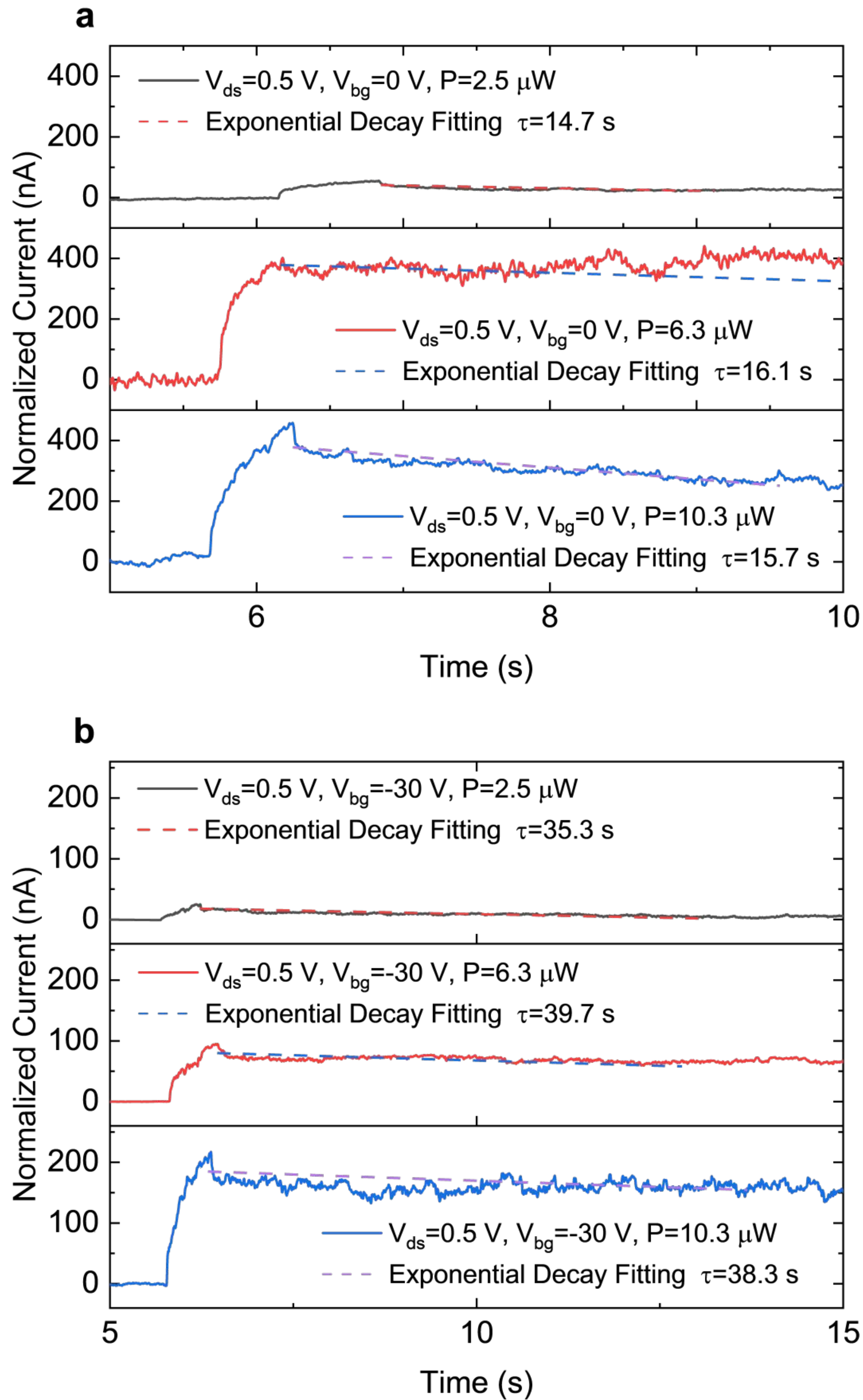


**Figure S3**. **Optical power–dependent photocurrent response.** Time-resolved photocurrent curves measured under different incident laser power densities while

keeping all electrical bias conditions unchanged. The photocurrent amplitude increases monotonically with increasing optical power, confirming that the device response originates from photogenerated carrier processes. Importantly, the overall decay dynamics remain nearly unchanged across different illumination powers, indicating that the underlying recombination mechanism governing the persistent photocurrent is independent of excitation intensity within the investigated range.

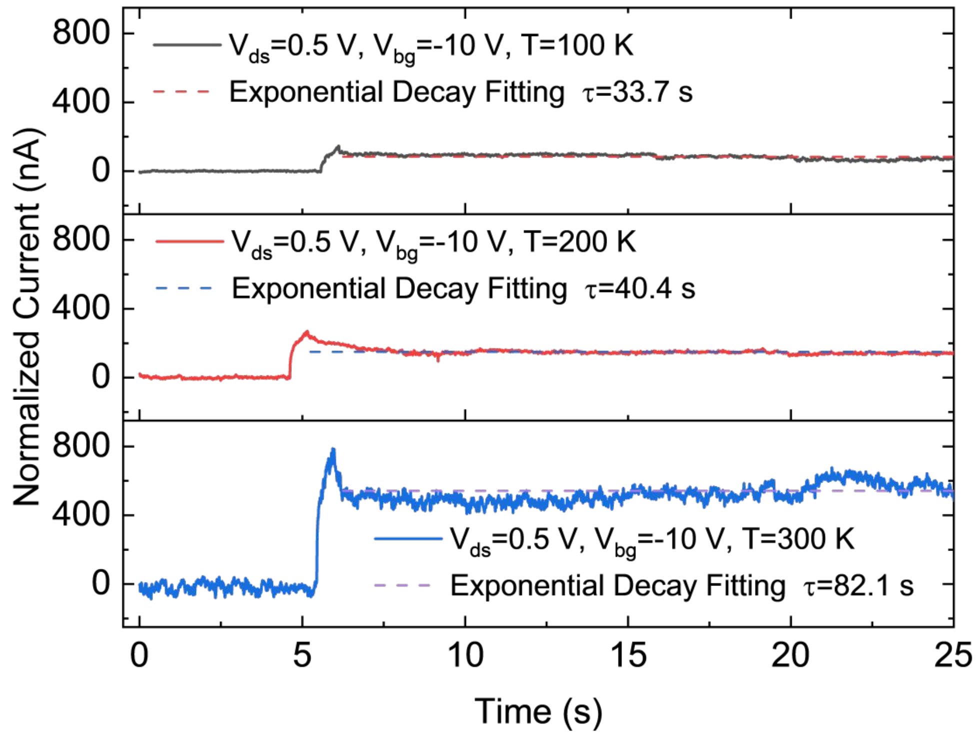


**Figure S4. Temperature-dependent photoresponse of the $MoS_2$–BP heterojunction device.** Time-resolved photocurrent measurements recorded at different temperatures (100 K, 200 K, and 300 K) under identical illumination conditions. The device exhibits similar photocurrent rise and decay characteristics over the entire temperature range, with only moderate variation in decay rate. The persistence of long-lived photocurrent at low temperatures indicates that the observed relaxation dynamics are governed primarily by intrinsic recombination processes within the heterojunction rather than by environmental adsorbate effects. These results support the thermally assisted recombination-induced current mechanism discussed in the main text.